Asian Journal of Chemistry; Vol. 37, No. 1 (2025), 61-68

ASIAN JOURNAL OF CHEMISTRY

https://doi.org/10.14233/ajchem.2025.32829

Synthesis and Characterization of $LaFeO_3$@ZnS Core-Shell Nanocomposites as Photocatalyst for the Degradation of Methylene Blue Dye

REEJA GOPALAKRISHNAN NAIR

Department of Physics, Government College Malappuram, Munduparamba P.O., Malappuram-676509, India

Corresponding author: E-mail: reejagnair10@gmail.com

Received: 3 October 2024; *Accepted*: 25 November 2024; *Published online*: 31 December 2024; AJC-21852

A two-step process involving hydrothermal and co-precipitation methods was used to synthesize core-shell nanoparticles of lanthanum ferrite @zinc sulphide ($LaFeO_3$@ZnS), which were then characterized. The X-ray diffraction (XRD) patterns exhibiting distinct diffraction peaks corresponding to both $LaFeO_3$ and ZnS components confirmed the synthesis of the nanocomposite. Transmission electron microscopy (TEM) images confirmed that the nanocomposite exhibited a core-shell structure. The photoluminescence quenching in $LaFeO_3$@ZnS nanoparticles indicates a decrease in the recombination of photogenerated charge carriers. The photocatalytic degradation of methylene blue was assessed using $LaFeO_3$@ZnS core-shell nanoparticles, which showed a considerable improvement in efficiency compared to the pure $LaFeO_3$ and ZnS nanoparticles. This superior photocatalytic performance can be attributed to the synergistic interaction between the $LaFeO_3$ core and ZnS shell, which led to increased absorption of visible light by the photocatalyst and longer lifetimes of the photogenerated charge carriers without undergoing recombination.

Keywords: Photocatalysis, Core-shell nanostructures, Lanthanum ferrite, Zinc sulphide, Methylene blue dye, Degradation.

INTRODUCTION

Industrial dyes are the major effluents that significantly contribute to water pollution, posing severe health and environmental risks [1,2]. Most of the dyes are complex organic compounds, aromatic in nature, engineered to maintain their colour despite exposure to water, sweat, light, various oxidizing and reducing chemicals and microbial activity [3]. As a result, they are extensively used in various industries such as textiles, food, rubber, printing, cosmetics, medicine, plastics and paper, all of which benefit from their durability and vivid colours [4]. However, the substantial volumes of dyed wastewater generated, present considerable hazard to the entire ecosystem. The challenges of efficiently cleaning and controlling such wastewater is further complicated by the toxicity and permanence of certain dyes. Various physical, biological and chemical methods are used for dye degradation [5-8]. However, physical methods such as ion-exchange, membrane separation and adsorption are often less favoured due to limitations like pore blockage and membrane fouling, which restrict their applicability and effectiveness [4,9-11]. On the other hand, biological methods using microbial and enzymatic techniques, though more environment friendly, tend to be less efficient due to their susceptibility to deactivation by various physical or chemical factors and the need for extended periods to achieve effective dye degradation [12-14]. Chemical wastewater treatment methods, including oxidation, electrolysis and coagulation-flocculation, are generally more efficient; however, these methods can produce toxic byproducts and generate sludge with disposal issues [15-17]. Moreover, they face commercialization challenges such as high energy consumption, large chemical requirements and the need for specialized equipments. In this light, advanced oxidation processes (AOPs) such as ozonation, Fenton reaction, ultrasound and photocatalytic processes have evolved as efficient strategies for dye removal [18-20].

Among these AOPs, photocatalytic dye degradation has been developed as a sustainable and effective technology where a catalyst upon photon irradiation promotes the complete mineralization of the hazardous dye into non-toxic compounds [21]. The major requirement of this technique is to identify and develop an optimal photocatalyst which is non-reactive with biological and chemical substances, resistant to degradation under light exposure, capable of utilizing visible or near-UV light, having increased catalytic active sites for the surface interface reactions, cost-effective, safe for human health and exhibiting high photocatalytic activity [22]. Till date, titanium dioxide (TiO_2) remains as the most extensively studied photocatalyst [23]. However, other metal oxides such as zinc oxide (ZnO), tungsten trioxide (WO_3), iron(III) oxide (Fe_2O_3), vanadium pentoxide (V_2O_5), silver oxide (Ag_2O), binary metal sulfide semiconductors like cadmium sulfide (CdS) and zinc sulfide (ZnS), perovskites like strontium titanate ($SrTiO_3$), bismuth ferrite ($BiFeO_3$) are also being investigated for their photocatalytic potential [24-26]. The effectiveness of these photocatalysts in processes like dye degradation is influenced by various physical properties, including particle size, shape, surface morphology, porosity, crystalline quality, specific surface area and the size of band gap [27,28]. However, weak absorption of visible light, rapid recombination of photogenerated charge carriers, poor surface/interface reactions and limited surface area continue to pose significant challenge that minimizes the quantum yield and restrict their viability for photocatalytic applications.

Nevertheless, in the recent years, there has been a notable rise in the development of specialized nanomaterials tailored for specific applications, with multifunctional capabilities, aimed to address the existing limitations and thereby improve the photocatalytic performance. Various approaches have been implemented for example, elemental doping that mainly alters the bandgap; cocatalyst loading that boosts the separation of photogenerated excitons and the morphological variation in enhancing the characteristics like specific surface area and light absorption [29-34]. Another suitable alternative is to couple different nanomaterials to form heterojunction nanocomposites [35,36]. Within the realm of nanocomposites, the core-shell nanostructure stands out as a distinct category, characterized by an arrangement in which the shell nanoparticle envelops the core nanoparticle. The main advantage of such nanostructures lies in their ability to merge the characteristics of both core and shell. This interaction facilitates the accurate adjustment of several features, such as porosity, crystallinity, specific surface area, charge carrier recom-bination time and band gap size [37].

Lanthanum ferrite is a visible light active, perovskite type material possessing a narrow bandgap of nearly 2 eV, making it a highly suitable photocatalyst for reactions initiated by visible light. Moreover, $LaFeO_3$ exhibits exceptional chemical and thermal stability, along with remarkable biocompatibility. However, fast recombination of excitons impedes its photocatalytic efficiency [38,39]. The shell nanoparticle, ZnS is a highly promising, non-toxic, earth abundant and cost effective photocatalyst with potential for considerable photocatalytic activity, particularly, in the degradation of organic pollutants and water purification. However, its broad band gap that reduces its responsiveness to visible light challenges its catalytic performance [40]. In the current study, a novel lanthanum ferrite @zinc sulphide ($LaFeO_3$@ZnS) core-shell nanostructure was synthesized *via* a two-step process (hydrothermal method for core and co-precipitation technique for shell fabrication) and also investigated the structural, morphological, microstructural, optical and photoluminescence properties of $LaFeO_3$@ZnS core shell nanoparticles. The photocatalytic degradation efficiency of the synthesized nanocomposite for methylene blue (MB) dye was also investigated.

EXPERIMENTAL

The analytical grade reagents used in this work were ferric nitrate nonahydrate ($Fe(NO_3)_3·9H_2O$, 98%; Fisher Scientific), lanthanum nitrate hexahydrate ($La(NO_3)_3·6H_2O$, 99.9%; Alfa Aesar), citric acid ($C_6H_8O_7$, 99.5%; Spectrochem), ethanol (99%; Hyman), zinc nitrate hexahydrate ($Zn(NO_3)_2·6H_2O$, 98%; Qualigens) and sodium sulphide (Na_2S, 98%; Fischer Scientific). Deionized water was used for the synthesis and photocatalytic experiments.

Synthesis of pristine $LaFeO_3$ nanoparticles: The $LaFeO_3$ nanoparticles (core) were synthesized by following a hydrothermal method [41]. Briefly, a 1:1 molar ratio of $Fe(NO_3)_3·9H_2O$ and $La(NO_3)_3·6H_2O$ were dissolved in ethanol-water mixture (1:1) volume ratio, to which citric acid (5 mL) was added slowly and stirred continuously for 30 min. An 80 mL Teflon lined autoclave was filled with the resultant mixture and kept at 180 ºC for 24 h. Once the reaction was completed, the autoclave was allowed to cool to room temperature. The resulting solid product was then collected, washed twice with absolute ethanol followed by distilled water and then, dried in a vacuum oven at 60 ºC for 12 h.

Synthesis of $LaFeO_3$@ZnS and pristine ZnS nanoparticles: The ZnS shell nanostructure was synthesized following co-precipitation technique [42]. A specified amount of as-synthesized $LaFeO_3$ was sonicated in 100 mL of deionized water for 1 h. Following this, 10 mL of one molar each Na_2S and $Zn(NO_3)_2·6H_2O$ were introduced dropwise to the dispersion, sequentially, and the mixture was stirred for 3 h. The resulting precipitate was washed several times with deion-ized water followed by ethanol and dried at 120 ºC. Pristine ZnS was also synthesized following the same route without adding $LaFeO_3$ powder.

Photocatalytic experiment: The photocatalyst nanocomposite (50 mg) were added to 100 mL of methylene blue (MB) solution at a concentration of 3 ppm. A 300 W xenon arc lamp was served as the light source. To establish the adsorption–desorption equilibrium, the dye solution containing the photocatalyst was stirred in the dark for 30 min. Subsequently, the sample was irradiated with UV-visible light from the Xe-Arc lamp while being magnetically stirred. At the intervals of 15 min, 4 mL samples were collected, centrifuged and the supernatant was analyzed. The change in MB concentration resulting from the photocatalytic activity of the nanocomposite was assessed by measuring the absorbance at 640 nm using a UV-Vis spectrometer.

Characterization: The structural and crystallographic characterization of $LaFeO_3$, ZnS and $LaFeO_3$@ZnS core-shell samples were carried out with an X-ray diffractometer (Rigaku 600) using a Cu$K\alpha$ source (λ = 1.542 Å). The morphology of $LaFeO_3$@ZnS core-shell nanostructures were examined using a scanning electron microscope (ZEISS GEMINI SEM 300) operating at 20 kV. The microstructure of the core-shell samples was analyzed employing transmission electron microscope

(TEM) (JEOL Japan, JEM-2100 Plus) operating at 200 kV. High-resolution transmission electron microscopy (HRTEM) images and selected area electron diffraction (SAED) patterns were also collected to investigate the *d*-spacing and crystallinity of the sample. The optical absorption spectrum of the powder samples was collected using an integrating-sphere equipped Diffuse reflectance spectrophotometer (JASCO V-750 spectrometer) where BaSO$_4$ served as the reference material. To assess the photocatalytic dye degradation, ultraviolet-visible (UV-Vis) spectroscopy of the samples was also conducted with a Jasco V-750 spectrometer. Photoluminescence (PL) analysis was performed using Perkin-Elmer LS-55 spectroflourimeter.

RESULTS AND DISCUSSION

Structural studies: Fig. 1. displays the X-ray diffraction (XRD) patterns for pristine LaFeO$_3$ and ZnS, along with the LaFeO$_3$@ZnS nanocomposite. The XRD patterns of the synthesized LaFeO$_3$@ZnS core–shell nanoparticles exhibit two sets of peaks, corresponding to LaFeO$_3$ core and ZnS shell. The strong and well-defined diffraction peaks observed at 2θ values of 26.5º, 30.7º, 43.9º, 52.0º, 70.4º and 72.6º are associated with the (101), (121), (220), (202), (230) and (141) planes of LaFeO$_3$ core in the orthorhombic phase. The peaks at 2θ values of 28.9º, 48.1º and 57.1º correspond to the (111), (220) and (311) planes of ZnS in its cubic phase. These reflections align with the standard powder diffraction patterns of LaFeO$_3$ and ZnS, as indicated by the ICDD data (ICDD- 00-037-1493 for LaFeO$_3$ and ICDD-00-005-0566 for ZnS). The prominent peaks observed in the XRD pattern of LaFeO$_3$@ZnS nanocomposite correspond to those of both LaFeO$_3$ and ZnS, further confirming the presence of both phases. The broadening of the diffraction peaks in the XRD patterns suggests that the size of nanoparticles are in the nanoscale range. The average crystalline sizes of LaFeO$_3$ and ZnS nanoparticles were determined from Scherrer's formula and found to be 27.17 nm and 4.91 nm, respectively [43]. However, due to the mixed phases of LaFeO$_3$ and ZnS, it is not feasible to determine the average crystalline size of the LaFeO$_3$@ZnS core-shell nanoparticles.

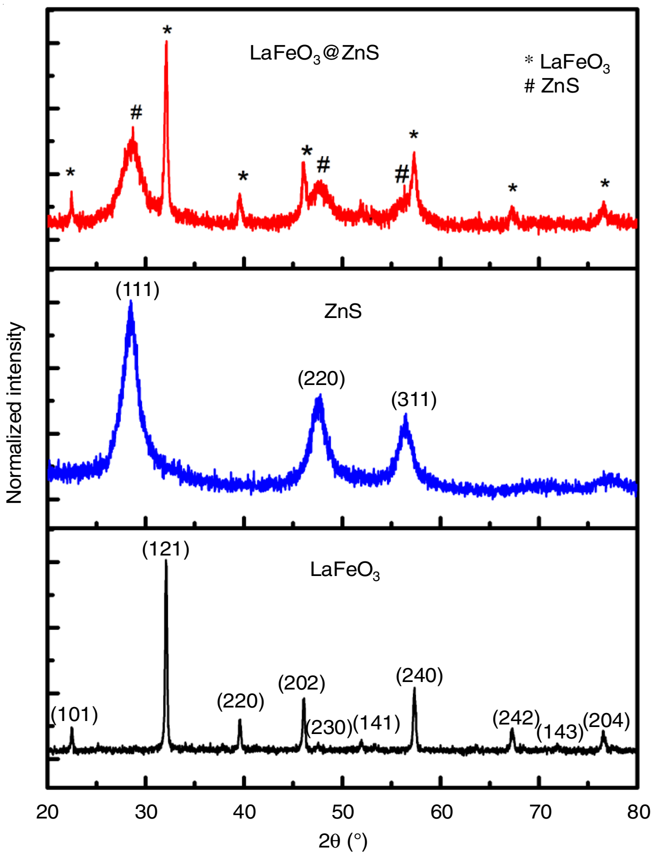

Fig. 1. XRD patterns of the LaFeO$_3$@ZnS, ZnS and LaFeO$_3$ samples

Morphological studies: Fig. 2 presents the images of the LaFeO$_3$ nanoparticles and LaFeO$_3$@ZnS photocatalyst, reve-

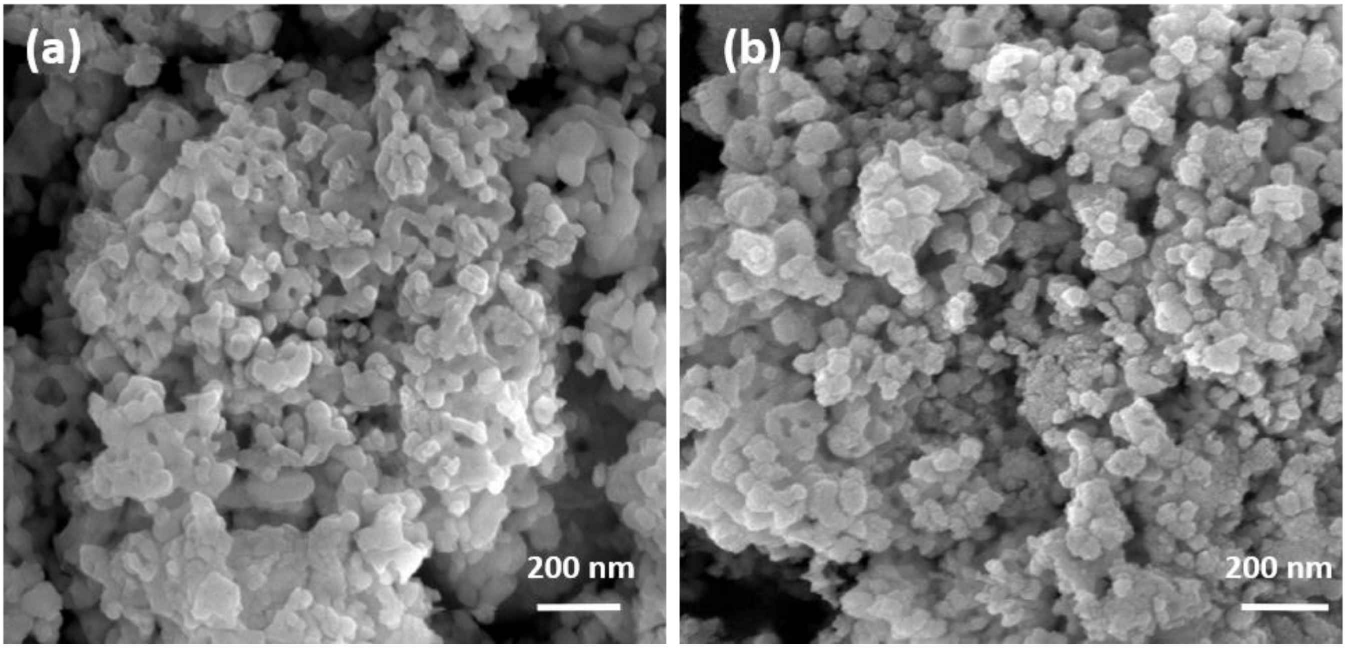

Fig. 2. SEM images of (a) LaFeO$_3$ core (b) LaFeO$_3$@ZnS core-shell nanoparticles

aling the surface morphology through scanning electron microscopy. In Fig. 2a, pristine $LaFeO_3$ nanoparticles display irregular structures with particle sizes in the range of a few hundred nanometers. In contrast in Fig. 2b, the nanocomposite shows slightly larger particles and a rough surface texture. The increased roughness of the nanocomposite is likely attributable to the encapsulation of ZnS nanoparticles onto the $LaFeO_3$ surface.

Microstructural studies: The microstructural analysis of the as-prepared samples were performed by TEM and HRTEM techniques. The TEM and HRTEM images of $LaFeO_3$@ZnS nanoparticles are shown in Fig. 3. The interface between $LaFeO_3$ core and ZnS shell is well distinguishable. The TEM images of $LaFeO_3$@ZnS nanoparticles (Fig. 3a-b) exhibit irregular shaped particles in which $LaFeO_3$ particles with sizes in the range of a 100 nm are surrounded by ZnS nanoparticles with particles size less than 10 nm, suggesting the formation of $LaFeO_3$@ZnS core-shell nanoparticles. Fig. 3c shows the HRTEM image of $LaFeO_3$@ZnS core-shell nanoparticles, which displays the lattice fringes of both $LaFeO_3$ and ZnS nanoparticles, with *d*-spacings of 0.258 nm and 0.311 nm, corresponding to the (121) and (111) lattice planes, respectively. The SAED spectra as shown in Fig. 3d, exhibits random spots which clearly reveals the polycrystalline nature of the particles. From the SAED pattern of $LaFeO_3$@ZnS core-shell NPs, the presence of (101), (121), (220), (202) and (240) planes of $LaFeO_3$ and (111) and (220) planes of ZnS are confirmed [44]. This indicates that the $LaFeO_3$ nanoparticles are closely interconnected with the ZnS nanoparticles. This intimate contact due to the establishment of a heterojunction, presumably, facilitate the transfer of photogenerated electrons and holes between $LaFeO_3$ and ZnS. As a result of this interaction, recombination is reduced, thereby improving the photocatalytic activity [45,46].

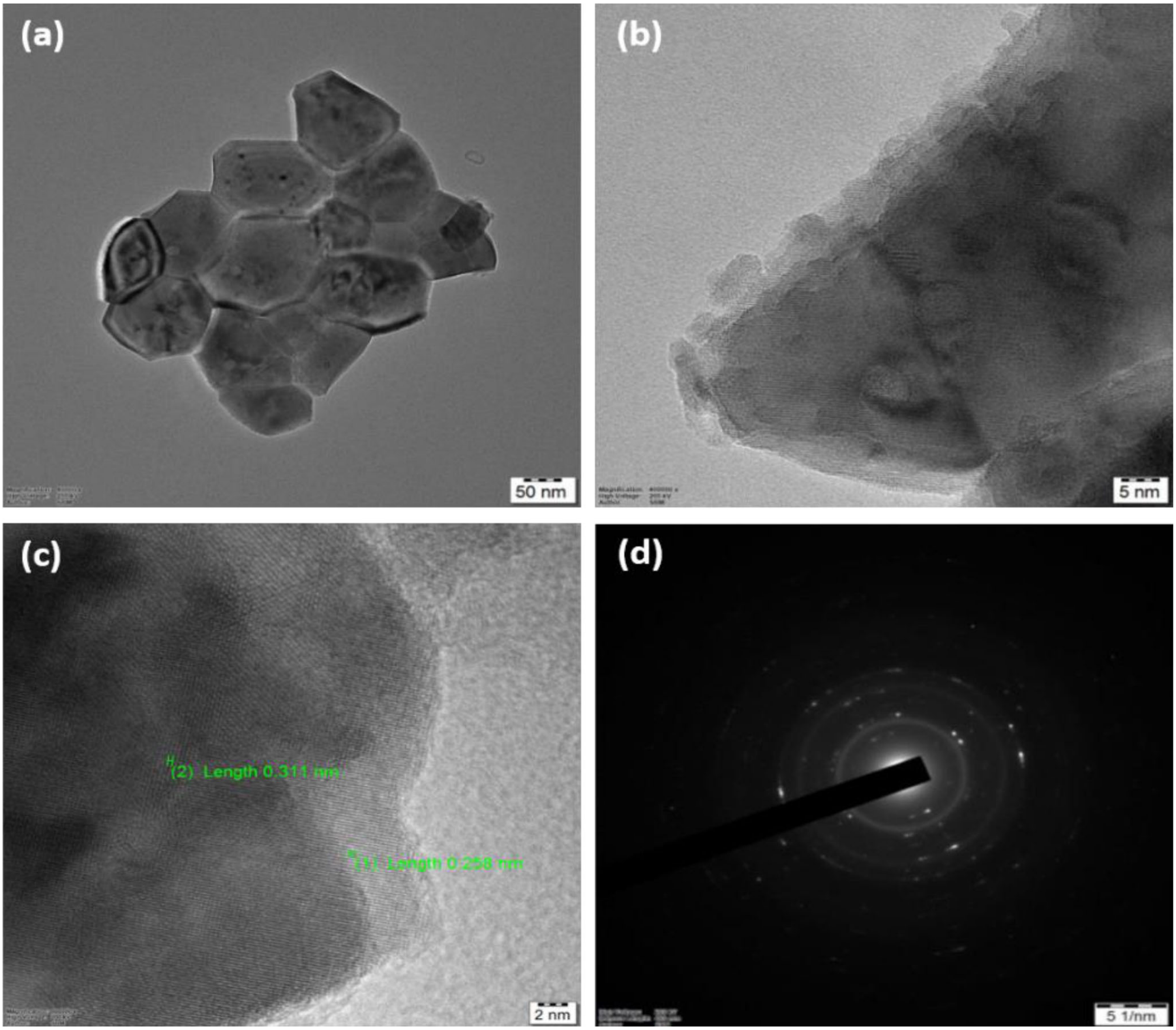

Fig. 3. TEM images of (a) and (b) $LaFeO_3$@ZnS core–shell nanoparticles revealing the encapsulation of the ZnS nanoparticles around the $LaFeO_3$ core (c) HRTEM image showing the d-spacings in the $LaFeO_3$@ZnS core-shell nanocomposite (d) SAED pattern of the $LaFeO_3$@ZnS core-shell nanocomposite

Elemental composition studies: The EDX analysis of synthesized $LaFeO_3$@ZnS nanocomposite revealed that all the elements, La, Fe and O belonging to the $LaFeO_3$ core and Zn and S present in the ZnS shell exist in $LaFeO_3$@ZnS nanoparticles (Fig. 4).

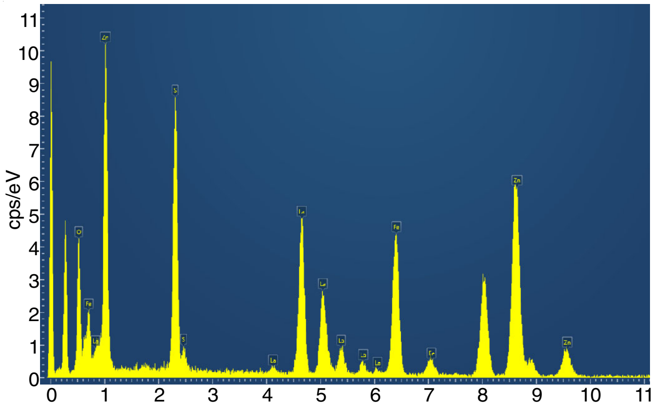

Fig. 4. TEM-EDX image of $LaFeO_3$@ZnS core–shell nanoparticles

Optical studies: The UV-visible absorption spectrum of the synthesized samples is presented in Fig. 5. Bare ZnS nanoparticles demonstrate absorption mainly in the UV spectrum with a threshold near 350 nm. In contrast, $LaFeO_3$ nanoparticles display a broader absorption range, extending into both the UV and visible regions. The encapsulation of $LaFeO_3$ nanoparticles by ZnS nanoparticles significantly enhances the absorption across the UV and visible spectrum, as evidenced by the UV-visible absorption data. Furthermore, FESEM analysis revealed a marked increase in surface roughness in the core-shell nanoparticles, which also likely contributed to the modified light absorption properties observed in the nanocomposite [47].

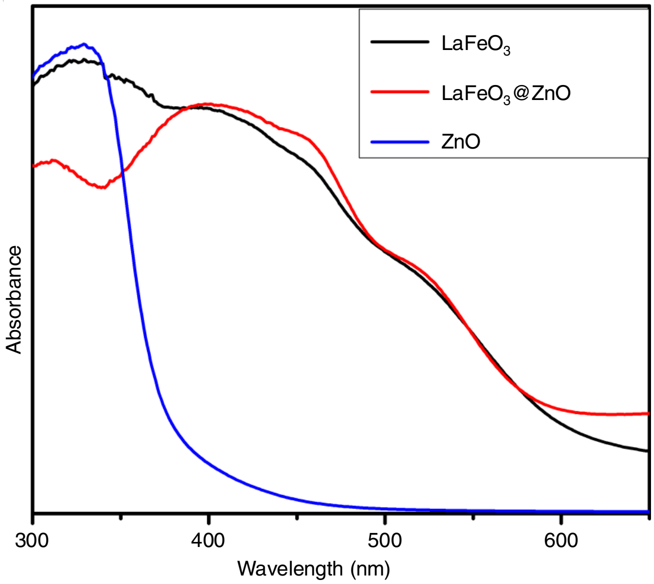

Fig. 5. UV-visible absorption spectrum of $LaFeO_3$, ZnS and $LaFeO_3$@ZnS core-shell nanocomposite

The band gap energy of the as-synthesized photocatalysts was determined using the Kubelka-Munk equation:

$$(F(R)h\nu)^n = k(h\nu - E_g)$$

where F(R) represents the Kubelka-Munk function as an approximation of the absorption coefficient and this is obtained from diffuse reflectance data, hν is the photon energy, E_g is the band gap energy of the sample and k is a proportionality constant [48]. In this equation, n is a constant that depends on the type of electronic transition thus for this study, n = 2 is adopted, indicating direct transitions. The band gap energy of the synthesized nanocomposite was estimated by extrapolating the linear portion of the $[F(R)h\nu]^2$ *versus* hν graph plot (Fig. 6). The estimated band gaps of ZnS and $LaFeO_3$ were 3.37 eV and 2.08 eV, respectively, with ZnS absorbing UV light and $LaFeO_3$ absorbing visible light, as observed in the UV-visible absorption spectrum. Thus, the optical band gap of $LaFeO_3$@ZnS core-shell nanostructure was found to be 2.25 eV, indicating successful formation of the core-shell structure, which effectively modifies the electronic structure and alters the optical properties of the material.

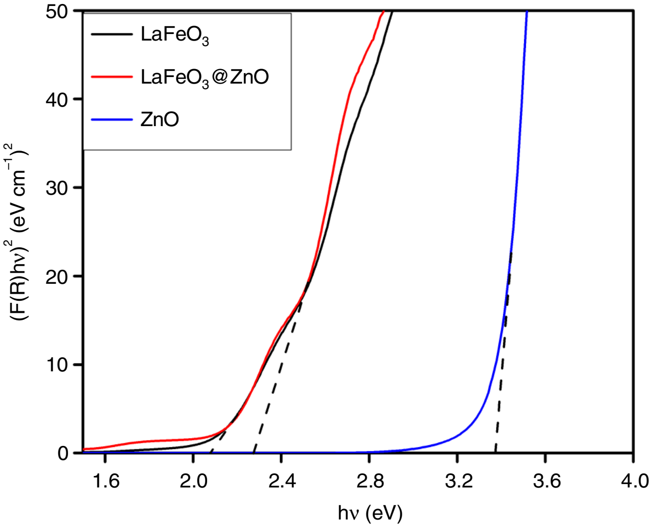

Fig. 6. The plot of $(F(R)h\nu)^2$ *versus* hν of $LaFeO_3$@ZnS core-shell nanostructure, $LaFeO_3$ and ZnS nanoparticles

Photoluminescence (PL) studies: To examine the migration of photogenerated electron-hole pairs between the two semiconductors, the photoluminescence (PL) spectra of bare ZnS, $LaFeO_3$ and $LaFeO_3$@ZnS using a 200 nm excitation wavelength at room temperature was analyzed (Fig. 7). The PL emission in ZnS nanomaterials originates from intrinsic defects such as sulfur vacancies, zinc vacancies and interstitials. The characteristic broadband emission between 410-470 nm (blue emission) is linked to the surface states of zinc sulfide, while electron transfer involving sulfur vacancies contributes to green emissions in the 500-550 nm range [49]. $LaFeO_3$ exhibits PL emission bands across the visible, with peaks at 412, 459, 488 and 529 nm, corresponding to transitions between defect states like oxygen vacancies and Fe^{3+} ions, as well as between the conduction and valence bands [39,50]. Remarkably, the PL intensity of $LaFeO_3$@ZnS core-shell nanostructure is significantly lower than that of both the $LaFeO_3$ core and ZnS shell materials. This reduced intensity is primarily due to suppressed

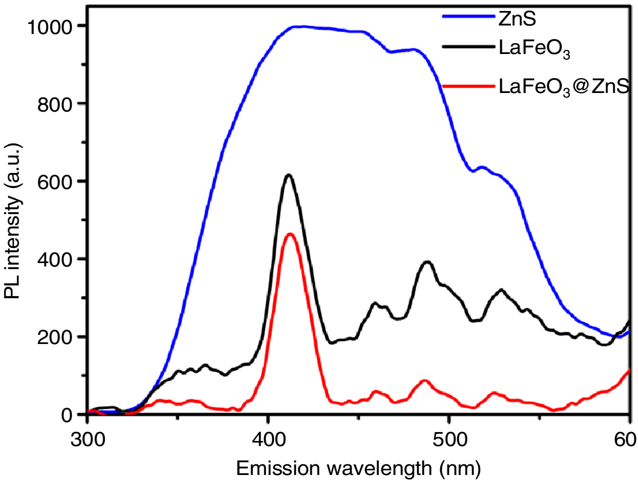

Fig. 7. PL spectra of synthesized $LaFeO_3$, ZnS and $LaFeO_3$@ZnS samples

recombination processes, as the core-shell heterojunction facilitates the lengthening of the lifetimes of photogenerated electron-hole pairs between $LaFeO_3$ and ZnS, enhancing their availability for photocatalytic activity [51]. Consequently, under visible light irradiation, the retention of photogenerated electron-hole pairs in $LaFeO_3$@ZnS nanoparticles is improved, leading to greater availability for photocatalytic degradation. This lower PL intensity explains the superior photocatalytic performance of the $LaFeO_3$@ZnS core-shell nanomaterial compared to other nanomaterials.

Photocatalytic activity: The photocatalytic performance of the synthesized nanostructures was evaluated by degrading methylene blue (MB) dye under UV-visible light irradiation. In this study, the simulated sunlight from a 300W Xe-Arc lamp was used and the initial concentration of MB dye was 3 ppm. The photocatalytic experiments were conducted at the natural pH of MB dye solution, under ambient temperature and pressure conditions. The degradation of MB solution was monitored using its UV-visible absorption spectrum. The UV-visible spectra of MB solution was obtained at different time intervals during the photocatalytic degradation process (Fig. 8).

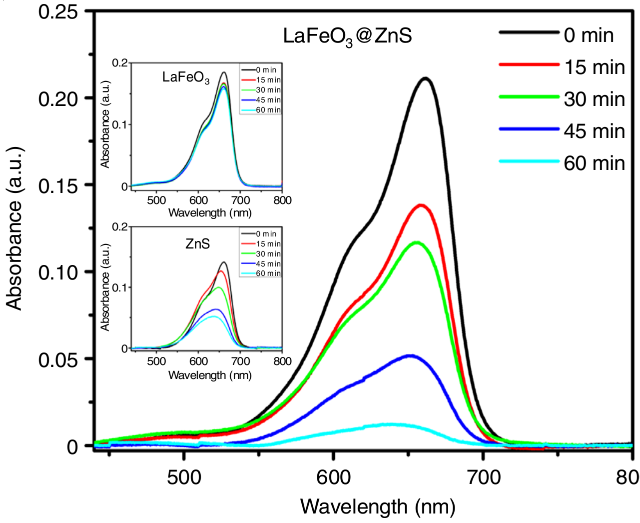

Fig. 8. UV-visible spectrum of MB dye during photocatalytic degradation in the presence of $LaFeO_3$@ZnS, $LaFeO_3$ and ZnS nanoparticles

The time-dependent degradation of MB dye in the presence of ZnS, $LaFeO_3$ and $LaFeO_3$@ZnS photocatalysts is shown in Fig. 9. Only 15% degradation was observed with the $LaFeO_3$ photocatalyst, while 63% degradation occurred with ZnS after 60 min of light irradiation. However, the $LaFeO_3$@ZnS photocatalyst achieved 100% degradation within the same time, demonstrating its superior photocatalytic activity compared to the bare ZnS and $LaFeO_3$ nanomaterials. This enhanced performance of the core-shell nanostructure can be attributed to its surface heterogeneity, optimal bandgap and efficient charge carrier transport within the core-shell structure.

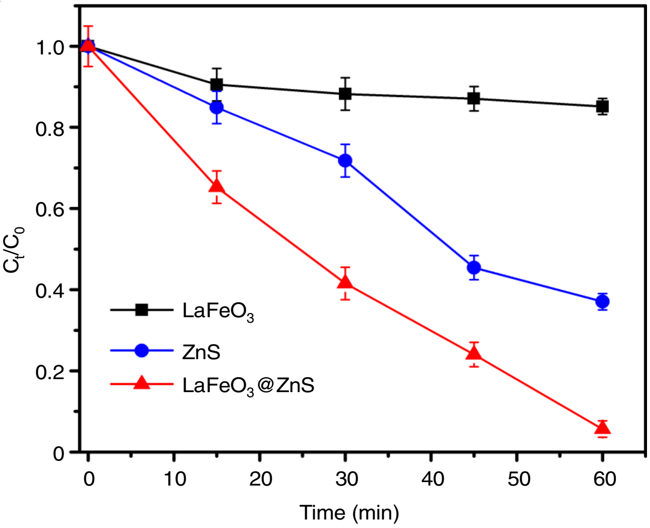

Fig. 9. The time dependent photocatalytic degradation of MB in presence of $LaFeO_3$, ZnS and $LaFeO_3$@ZnS photocatalysts

To understand the photocatalytic processes, the kinetic catalytic degradation of MB solution was analyzed using the Langmuir-Hinshelwood model [52,53], which is represented as follows:

$$-\frac{dC}{dt} = \frac{kKC}{1+KC_0} \tag{2}$$

where k and K are the constants of reaction rate (mg L^{-1} min^{-1}) and adsorption equilibrium (L mg^{-1}), respectively. In highly diluted solution of dye, the term 'KC_0' becomes less than 1, $KC_0 << 1 \rightarrow 1 + KC_0 \approx 1$. Then, eqn. 2 can be rewritten as follows:

$$-\frac{dC}{dt} = kKC \tag{3}$$

$$\frac{dC}{dt} = k_{app}C$$

Considering $k_{app} \approx kK$ as the apparent rate constant of the reaction, the above equation representing the pseudo-first order reaction kinetics as $C_t = C_0e^{-k_{app}t}$ [54]. Thus, the apparent rate constant of the reaction k_{app} can be obtained by estimating the slope of linear fit of $\ln(C_0/C_t)$ *versus* time (t) (Fig. 10). The half-life of the photocatalytic reaction can be calculated using the equation $T_{1/2} = \ln 2/k$, where k is the reaction rate constant [55]. The estimated values of the rate constant and the corresponding half-life for the photocatalytic reactions are presented in Table-1.

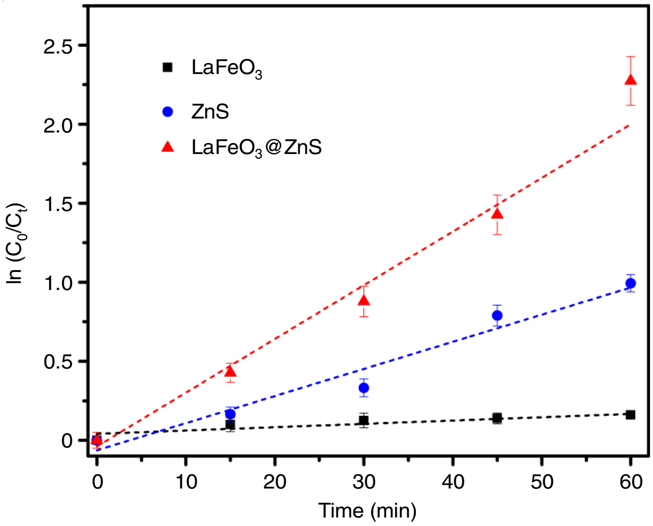

Fig. 10. The linear fit of the pseudo-first-order kinetic reaction. All the photocatalytic reactions show a good fit to this model

TABLE-1
THE RATE CONSTANT AND HALF-LIFE VALUES OF THE PHOTOCATALYTIC REACTIONS

Photocatalyst	Rate constant ($\times 10^{-2}$ min^{-1})	Half-life of the reaction ($\times 10^{2}$ min)
ZnS	1.71 ± 0.18	0.40 ± 0.10
$LaFeO_3$	0.21 ± 0.01	3.30 ± 0.04
$LaFeO_3$@ZnS	3.39 ± 0.27	0.20 ± 0.07

The reaction rate constants reveal that the photocatalytic reaction using $LaFeO_3$@ZnS core-shell nano-structure is approximately 16 times faster than with bare $LaFeO_3$ and about twice as fast as with bare ZnS. Similarly, half of MB dye molecules degrade after 20 min of light irradiation with $LaFeO_3$@ ZnS, compared to 40 min with ZnS and 330 min with $LaFeO_3$. Thus, it can be concluded that the core-shell nanostructure offers an efficient and superior photocatalytic activity towards the degradation of MB dye. Thus, the enhanced photocatalytic activity of $LaFeO_3$@ZnS core-shell nanocomposite when compared to bare $LaFeO_3$ and ZnS nanoparticles can be due to its surface inhomogeneity, good visible light sensitivity and *in situ* heterojunction formation resulting in an internal electric field, preventing the charge carrier recombination.

Conclusion

In this study, $LaFeO_3$ nanoparticles were synthesized using a hydrothermal method and subsequently combined with ZnS nanoparticles to develop a novel $LaFeO_3$@ZnS core-shell nanocomposite through a co-precipitation technique. The formation of the nanocomposite was confirmed by X-ray diffraction (XRD) and energy dispersive X-ray spectroscopy (EDX). The TEM images demonstrated the core-shell structure of the synthesized composite, while SEM images indicated that the $LaFeO_3$@ZnS core-shell nanocomposite exhibits surface roughness. The core shell photocatalyst was found to be active under visible light, with a bandgap of 2.25 eV, as determined from the Tauc plot. The observed photoluminescence quenching in $LaFeO_3$@ZnS nanoparticles suggests a reduction in the recombination of photogenerated charge carriers. Compared to the individual $LaFeO_3$ and ZnS nanoparticles, $LaFeO_3$@ZnS nanocomposite as photocatalyst displayed enhanced photodegradation of methylene blue (MB), achieving 100% removal of 3 ppm MB after 60 min of photoreaction. Factors contributing to this improved photocatalytic performance include surface heterogeneity, a broad absorption range extending into the visible and UV regions and the formation of an internal electric field which promotes the electron-hole separation. Moreover, the non-toxic and abundantly available nature of the $LaFeO_3$ core and ZnS shell materials suggests potential for the scalability of this photocatalyst for water remediation.

CONFLICT OF INTEREST

The authors declare that there is no conflict of interests regarding the publication of this article.

REFERENCES

1. A.M.S. Jorge, K.K. Athira, M.B. Alves, R.L. Gardas and J.F.B. Pereira, *J. Water Process Eng*., **55**, 104125 (2023); https://doi.org/10.1016/j.jwpe.2023.104125
2. D.A. Yaseen and M. Scholz, *Int. J. Environ. Sci. Technol*., **16**, 1193 (2019); https://doi.org/10.1007/s13762-018-2130-z
3. S. Suresh, *Curr. Environ. Eng*., **1**, 162 (2015); https://doi.org/10.2174/2212717801666141021235246
4. A.M. Subhi, J.A. Al-Najar and W.A.H. Noori, *Glob. NEST J.*, **24**, 451 (2022); https://doi.org/10.30955/gnj.004325
5. M. Tripathi, S. Singh, S. Pathak, J. Kasaudhan, A. Mishra, S. Bala, D. Garg, R. Singh, P. Singh, P.K. Singh, A.K. Shukla and N. Pathak, *Toxics*, **11**, 940 (2023); https://doi.org/10.3390/toxics11110940
6. C. Kathing and G. Saini, *Recent Progr. Mater.*, **4(4)**, 1 (2022); https://doi.org/10.21926/rpm.2204028
7. P. Ahuja, S.K. Ujjain, R. Kanojia and P. Attri, *J. Compos. Sci*., **5**, 82 (2021); https://doi.org/10.3390/jcs5030082
8. D. Bhatia, N.R. Sharma, J. Singh and R.S. Kanwar, *Crit. Rev. Environ. Sci. Technol.*, **47**, 1836 (2017); https://doi.org/10.1080/10643389.2017.1393263
9. G.E. Üstün, S.K.A. Solmaz and A. Birgül, *Resour. Conserv. Recycling*, **52**, 425 (2007); https://doi.org/10.1016/j.resconrec.2007.05.006
10. C.H. Liu, J.S. Wu, H.C. Chiu, S.Y. Suen and K.H. Chu, *Water Res.*, **41**, 1491 (2007); https://doi.org/10.1016/j.watres.2007.01.023
11. M.T. Yagub, T.K. Sen, S. Afroze and H.M. Ang, *Adv. Colloid Interface Sci.*, **209**, 172 (2014); https://doi.org/10.1016/j.cis.2014.04.002
12. E. Khelifi, H. Bouallagui, Y. Touhami, J.J. Godon and M. Hamdi, *Desalination Water Treat.*, **2**, 310 (2009); https://doi.org/10.5004/dwt.2009.294
13. J. Kanagaraj, T. Senthilvelan and R.C. Panda, *Clean Technol. Environ. Policy*, **17**, 1443 (2015); https://doi.org/10.1007/s10098-014-0869-6
14. A. Pandey, P. Singh and L. Iyengar, *Int. Biodeterior. Biodegradation*, **59**, 73 (2007); https://doi.org/10.1016/j.ibiod.2006.08.006
15. Y. Su, D. Jassby, S. Song, X. Zhou, H. Zhao, J. Filip, E. Petala and Y. Zhang, *Environ. Sci. Technol.*, **52**, 6466 (2018); https://doi.org/10.1021/acs.est.8b00231
16. L.N. Ukiwe, S.I. Ibeneme, C.E. Duru, B.N. Okolue, G.O. Onyedika and C.A. Nweze, *J. Adv. Chem.*, **9**, 2321 (2014); https://doi.org/10.24297/jac.v9i3.1006
17. M. Riera-Torres, C. Gutiérrez-Bouzán and M. Crespi, *Desalination*, **252**, 53 (2010); https://doi.org/10.1016/j.desal.2009.11.002

18. M. Priyadarshini, I. Das, M.M. Ghangrekar and L. Blaney, *J. Environ. Manage.*, **316**, 115295 (2022); https://doi.org/10.1016/j.jenvman.2022.115295
19. C.C. Amorim, M.M.D. Leão, R.F.P.M. Moreira, J.D. Fabris and A.B. Henriques, *Chem. Eng. J.*, **224**, 59 (2013); https://doi.org/10.1016/j.cej.2013.01.053
20. S. Jayaraman and A.R. Warrier, *Mater. Chem. Phys.*, **278**, 125610 (2022); https://doi.org/10.1016/j.matchemphys.2021.125610
21. Z.H. Jabbar and B.H. Graimed, *J. Water Process Eng.*, **47**, 102671 (2022); https://doi.org/10.1016/j.jwpe.2022.102671
22. A.O. Ibhadon and P. Fitzpatrick, *Catalysts*, **3**, 189 (2013); https://doi.org/10.3390/catal3010189
23. M. Pawar, S. Topcu Sendoðdular and P. Gouma, *J. Nanomater.*, **2018**, 5953609 (2018); https://doi.org/10.1155/2018/5953609
24. S. Gautam, H. Agrawal, M. Thakur, A. Akbari, H. Sharda, R. Kaur and M. Amini, *J. Environ. Chem. Eng.*, **8**, 103726 (2020); https://doi.org/10.1016/j.jece.2020.103726
25. S. Munyai and N.C. Hintsho-Mbita, *Curr. Res. Green Sustain. Chem.*, **4**, 100163 (2021); https://doi.org/10.1016/j.crgsc.2021.100163
26. L. Huang, X. Huang, J. Yan, Y. Liu, H. Jiang, H. Zhang, J. Tang and Q. Liu, *J. Hazard. Mater.*, **442**, 130024 (2023); https://doi.org/10.1016/j.jhazmat.2022.130024
27. H. Jindal, D. Kumar, M. Sillanpaa and M. Nemiwal, *Inorg. Chem. Commun.*, **131**, 108786 (2021); https://doi.org/10.1016/j.inoche.2021.108786
28. M.A. Hassaan, M.A. El-Nemr, M.R. Elkatory, S. Ragab, V.-C. Niculescu and A. El Nemr, *Top. Curr. Chem.*, **381**, 31 (2023); https://doi.org/10.1007/s41061-023-00444-7
29. A.S.M. Nur, M. Sultana, A. Mondal, S. Islam, F.N. Robel, A. Islam and M.S.A. Sumi, *J. Water Process Eng.*, **47**, 102728 (2022); https://doi.org/10.1016/j.jwpe.2022.102728
30. Z. Mirzaeifard, Z. Shariatinia, M. Jourshabani and S.M. Rezaei Darvishi, *Ind. Eng. Chem. Res.*, **59**, 15894 (2020); https://doi.org/10.1021/acs.iecr.0c03192
31. M. Abd Elkodous, A.M. El-Khawaga, M.M. Abouelela and M.I.A. Abdel Maksoud, *Sci. Rep.*, **13**, 6331 (2023); https://doi.org/10.1038/s41598-023-33249-1
32. Y. Wang, M. Sun, Y. Fang, S. Sun and J. He, *J. Mater. Sci.*, **51**, 779 (2016); https://doi.org/10.1007/s10853-015-9401-6
33. N.M. Flores, U. Pal, R. Galeazzi and A. Sandoval, *RSC Adv.*, **4**, 41099 (2014); https://doi.org/10.1039/C4RA04522J
34. S.B. Khan, M. Hou, S. Shuang and Z. Zhang, *Appl. Surf. Sci.*, **400**, 184 (2017); https://doi.org/10.1016/j.apsusc.2016.12.172
35. H. Yang, *Mater. Res. Bull.*, **142**, 111406 (2021); https://doi.org/10.1016/j.materresbull.2021.111406
36. J. Low, J. Yu, M. Jaroniec, S. Wageh and A.A. AlGhamdi, *Adv. Mater.*, **29**, 1601694 (2017); https://doi.org/10.1002/adma.201601694
37. Q. Zhang, I. Lee, J.B. Joo, F. Zaera and Y. Yin, *Acc. Chem. Res.*, **46**, 1816 (2013); https://doi.org/10.1021/ar300230s
38. T. Ren, Z. Jin, J. Yang, R. Hu, F. Zhao, X. Gao and C. Zhao, *J. Hazard. Mater.*, **377**, 195 (2019); https://doi.org/10.1016/j.jhazmat.2019.05.070
39. M. Humayun, H. Ullah, M. Usman, A. Habibi-Yangjeh, A.A. Tahir, C. Wang and W. Luo, *J. Energy Chem.*, **66**, 314 (2022); https://doi.org/10.1016/j.jechem.2021.08.023
40. J.E. Samaniego-Benitez, L. Lartundo-Rojas, A. García-García, H.A. Calderón and A. Mantilla, *Catal. Today*, **360**, 99 (2021); https://doi.org/10.1016/j.cattod.2019.08.011
41. T. Zhang, Y. Guo, C. Li, Y. Li, J. Li, F. Zhao and H. Ma, *Adv. Powder Technol.*, **31**, 4510 (2020); https://doi.org/10.1016/j.apt.2020.09.027
42. P.S. Yoo, D. Amaranatha Reddy, Y.F. Jia, S.E. Bae, S. Huh and C. Liu, *J. Colloid Interface Sci.*, **486**, 136 (2017); https://doi.org/10.1016/j.jcis.2016.09.066
43. F.T.L. Muniz, M.A.R. Miranda, C. Morilla dos Santos and J.M. Sasaki, *Acta Crystallogr. A Found. Adv.*, **72**, 385 (2016); https://doi.org/10.1107/S205327331600365X
44. J.Y. Cheong, J.H. Chang, C. Kim, J. Lee, Y.S. Shim, S.J. Yoo, J.M. Yuk and I.D. Kim, *ACS Appl. Energy Mater.*, **2**, 2004 (2019); https://doi.org/10.1021/acsaem.8b02103
45. J. Yu, J. Zhang and S. Liu, *J. Phys. Chem. C*, **114**, 13642 (2010); https://doi.org/10.1021/jp101816c
46. C. Mondal, A. Singh, R. Sahoo, A.K. Sasmal, Y. Negishi and T. Pal, *New J. Chem.*, **39**, 5628 (2015); https://doi.org/10.1039/C5NJ00128E
47. L. Scholtz, L. Ladanyi and J. Mullerova, *AEEE*, **12**, 631 (2015); https://doi.org/10.15598/aeee.v12i6.1078
48. M.L. Myrick, M.N. Simcock, M. Baranowski, H. Brooke, S.L. Morgan and J.N. McCutcheon, *Appl. Spectrosc. Rev.*, **46**, 140 (2011); https://doi.org/10.1080/05704928.2010.537004
49. X. Wang, J. Shi, Z. Feng, M. Li and C. Li, *Phys. Chem. Chem. Phys.*, **13**, 4715 (2011); https://doi.org/10.1039/c0cp01620a
50. H. Shen, T. Xue, Y. Wang, G. Cao, Y. Lu and G. Fang, *Mater. Res. Bull.*, **84**, 15 (2016); https://doi.org/10.1016/j.materresbull.2016.07.024
51. A.A. Hoseini, S. Farhadi, A. Zabardasti and F. Siadatnasab, *RSC Advances*, **9**, 24489 (2019); https://doi.org/10.1039/C9RA04265B
52. M.F. Mubarak, H. Selim and R. Elshypany, *J. Environ. Health Sci. Eng.*, **20**, 265 (2022); https://doi.org/10.1007/s40201-021-00774-y
53. M. Ding, N. Yao, C. Wang, J. Huang, M. Shao, S. Zhang, P. Li, X. Deng and X. Xu, *Nanoscale Res. Lett.*, **11**, 205 (2016); https://doi.org/10.1186/s11671-016-1432-7
54. D. Tekin, H. Kiziltas and H. Ungan, *J. Mol. Liq.*, **306**, 112905 (2020); https://doi.org/10.1016/j.molliq.2020.112905
55. G. Rytwo and A.L. Zelkind, *Catalysts*, **12**, 24 (2021); https://doi.org/10.3390/catal12010024